Supplementary Information (SI) for Journal of Materials Chemistry C.

Supporting Information

Optoelectronic Synaptic Devices Based on Solution-Processed Microcrystal Indium Gallium Zinc Oxide for Neuromorphic Computing and Visual Perception

Shuangshuang Wu[1], Zhemi Xu[1,*], Zhigang Zhang[2], Jun Xu[2], Kun Bu[3], Feng Xu[2], Tianhao Ji[1,*], Liyang Pan[2,*]

1. School of Light Industry Science and Engineering, Beijing Technology and Business University, 100048, Beijing, China
2. School of Integrate Circuits, Tsinghua University, 100084, Beijing, China
3. School of Physics and Optoelectronic Engineering, Shandong University of Technology, 255000, Zibo, China

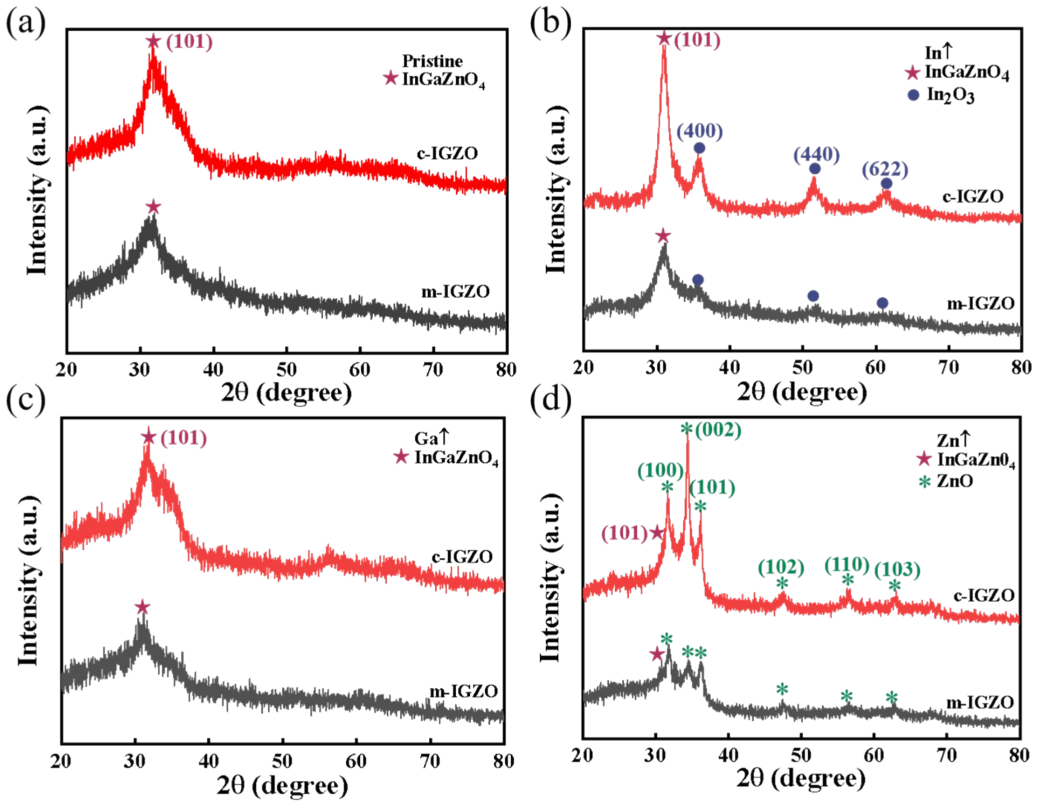

Figure S1. XRD Comparison of Microcrystalline and Crystalline Structures of (a) pristine, (b) In↑, (c) Ga↑, and (d) Zn↑ thin films.

The m-IGZO film was prepared by calcination at 300 °C for 0.5 hours, with three layers being deposited, while the c-IGZO film was obtained by calcination at 550 °C for 1 hour, also with three layers deposited. Upon comparison, it was found that for all components (including Pristine, In↑, Ga↑, and Zn↑), the crystalline films exhibited stronger XRD diffraction peak intensities than the microcrystalline films, with all characteristic peak positions remaining stable. The different components of the films revealed distinct phase orientations of In_2O_3, InGaZnO4, and ZnO_2.

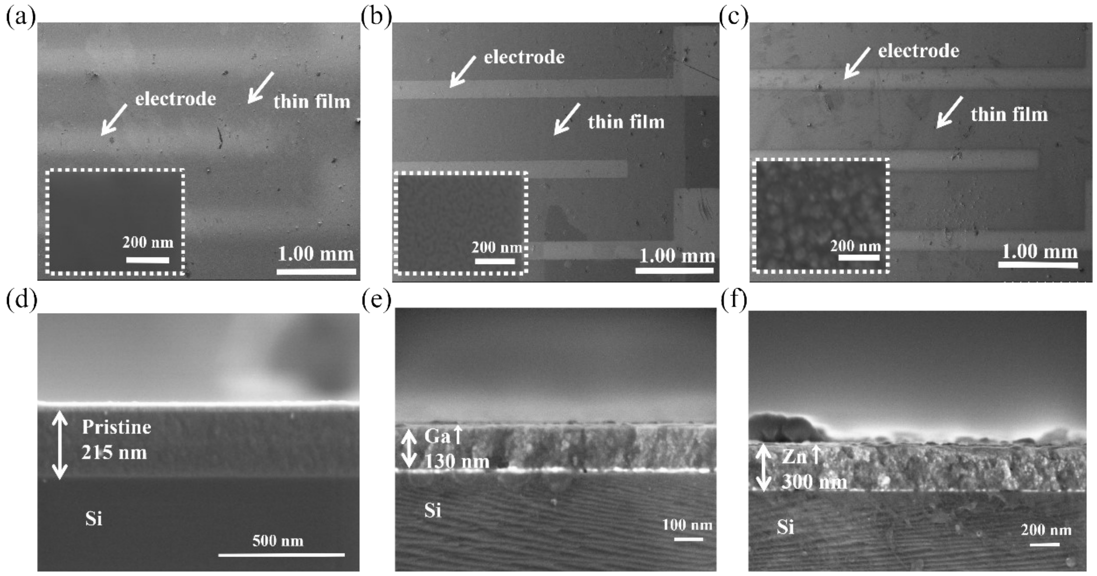

Figure S2. The SEM exterior view of (a) pristine, (b) Ga↑, and (c) Zn↑ thin films. Cross-sectional SEM image of (d) pristine, (e) Ga↑, and (f) Zn↑ devices.

Table S1. Comparison of elemental ratios (In, Ga, Zn, O) in pristine, In↑, Ga↑, and Zn↑ devices.

Sample	In (At.%)	Ga (At.%)	Zn (At.%)	O (At.%)
Pristine	13.2	8.7	12.5	65.5
In↑	19.7	6.0	7.5	66.9
Ga↑	8.5	16.3	9.1	66.1
Zn↑	12.4	5.9	15.5	66.2

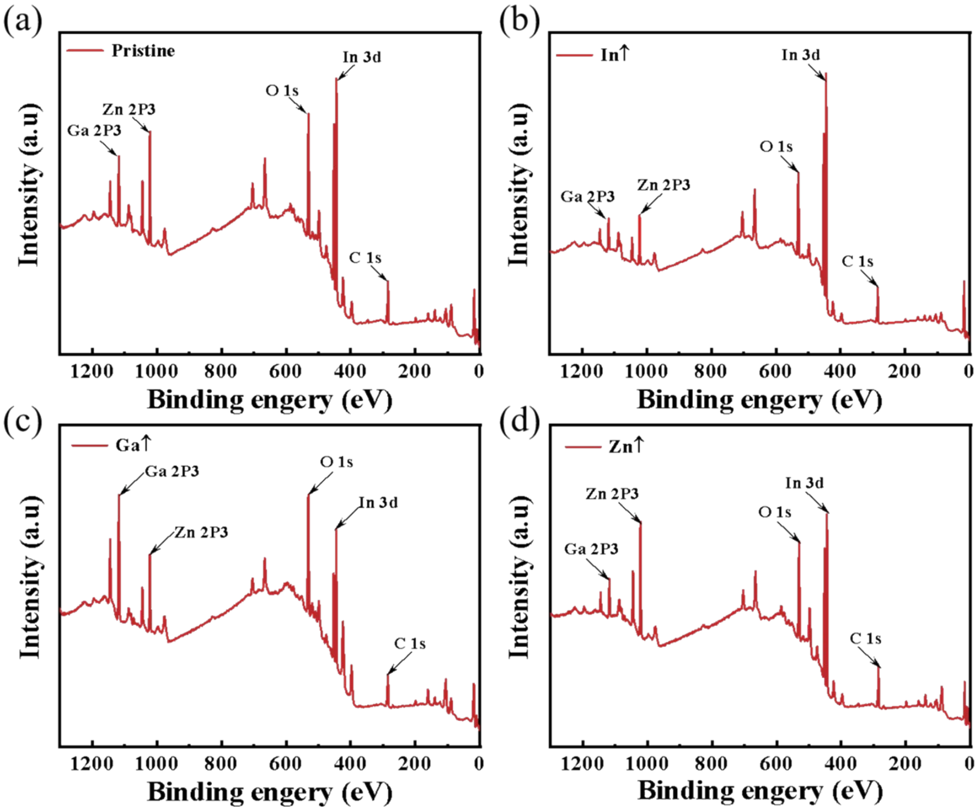

Figure S3. XPS survey spectra of (a) pristine, (b) In↑, (c) Ga↑, and (d) Zn↑ thin films.

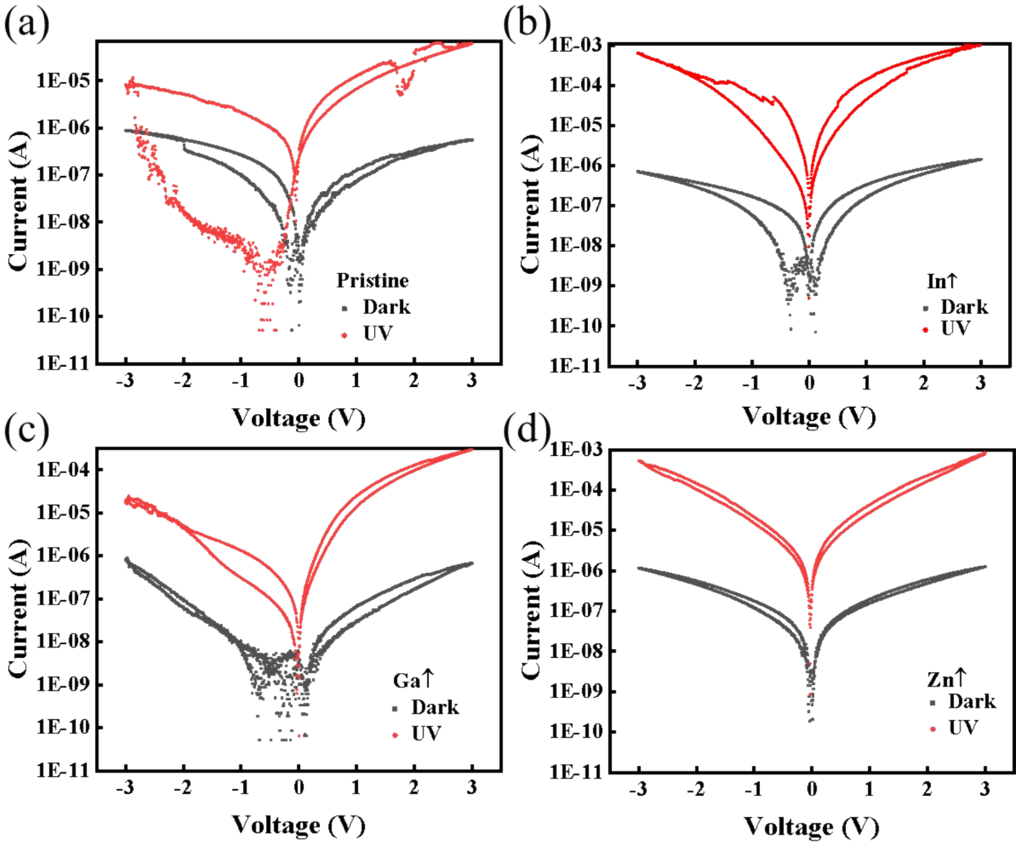

Figure S4. The I-V curves comparison of (a) pristine, (b) In↑, (c) Ga↑, (d) Zn↑, devices under dark and light conditions (1062 mW cm^{-2}).

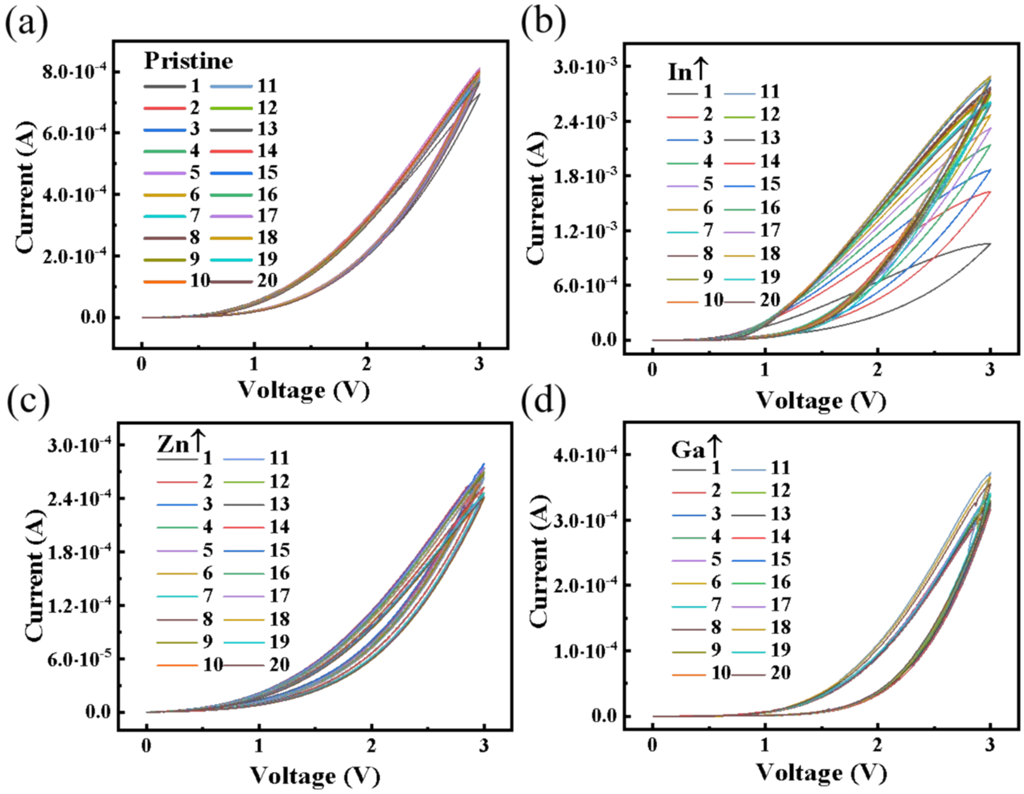

Figure S5. The I-V curves of the (a) pristine, (b) In↑, (c) Zn↑, (d) Ga↑ devices for 20 cycles under consecutive positive sweeping voltage (0 V→3 V→0 V).

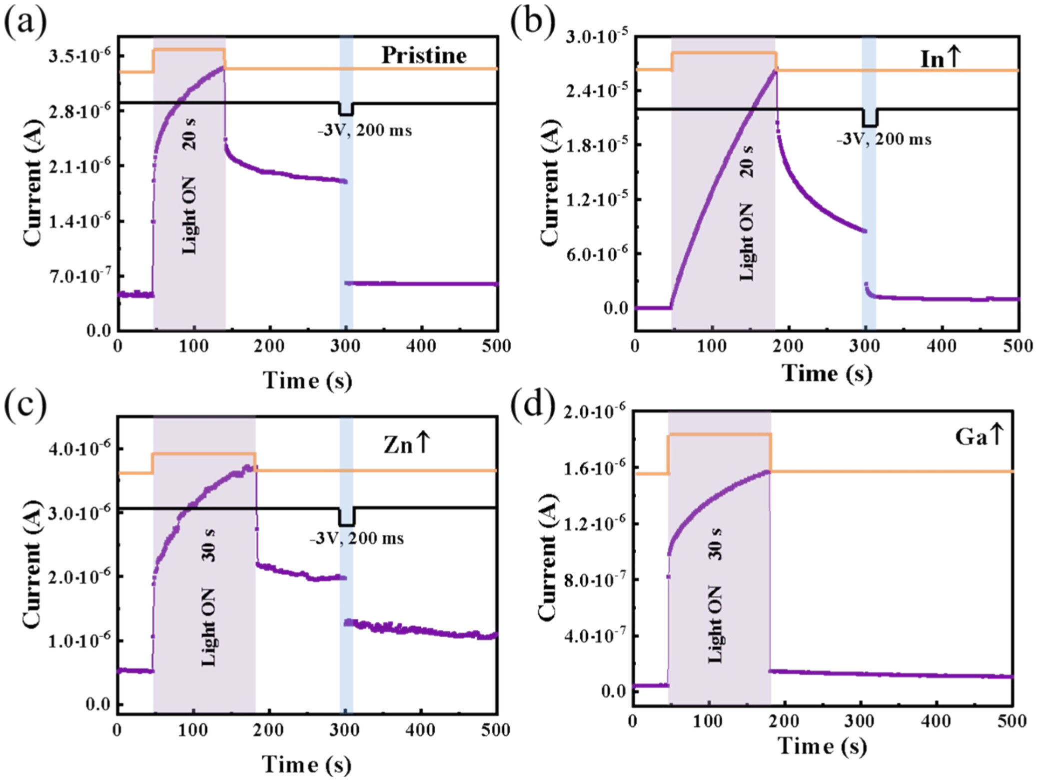

Figure S6. (a) The light-potentiation process with a single light pulse (intensity: 1062 mW cm^{-2}, duration: 20 s, marked by a purply colored area), and the electrical erase process with a voltage pulse (amplitude: -3 V, duration: 200 ms) of the pristine device. The light-potentiation process with a single light pulse (intensity: 1062 mW cm^{-2}, duration: 30 s, marked by a purply colored area), and the electrical erase process with a voltage pulse (amplitude: -3 V, duration: 200 ms) of (b) In↑, (c) Zn↑, (d) Ga↑ devices.

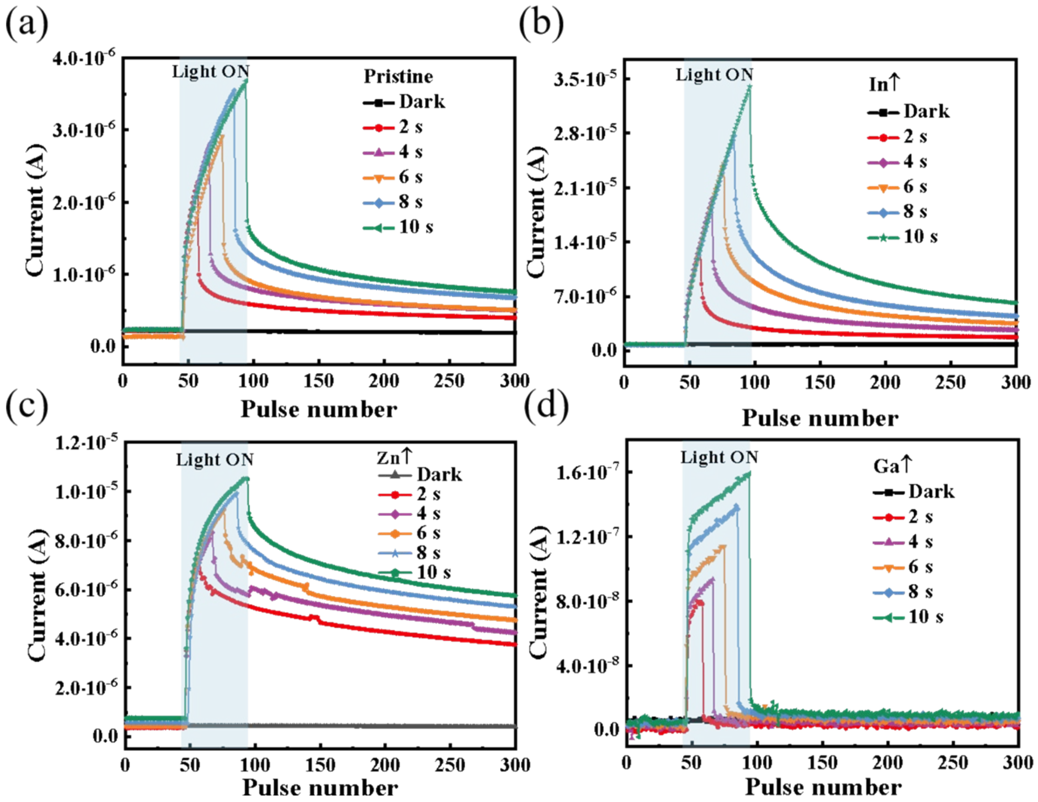

Figure S7. Current response of (a) Pristine, (b) In↑, (c) Zn↑, (d) Ga↑ devices under the light for 1062 mW cm^{-2} with various light durations (0 s, 2 s, 4 s, 6 s, 8 s, 10 s).

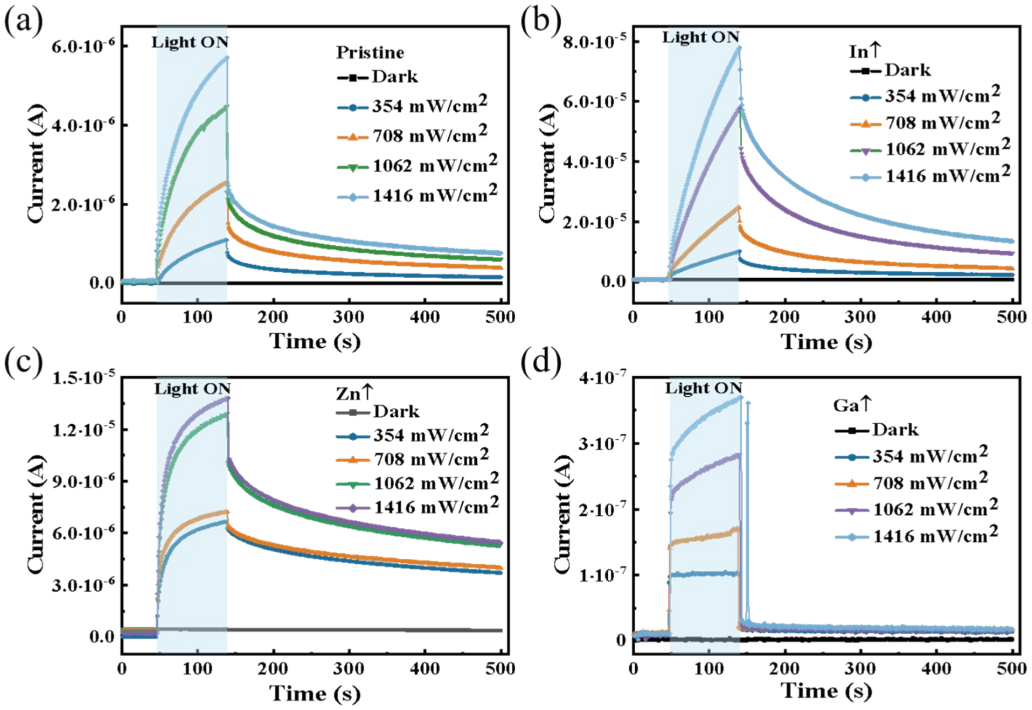

Figure S8. Current response under the light for 20 s of (a) pristine, (b) In↑, (c) Zn↑, and (d) Ga↑ devices with various light intensities (dark, 354, 708, 1062, 1416 mW cm^{-2}), followed by current decay after light is off.

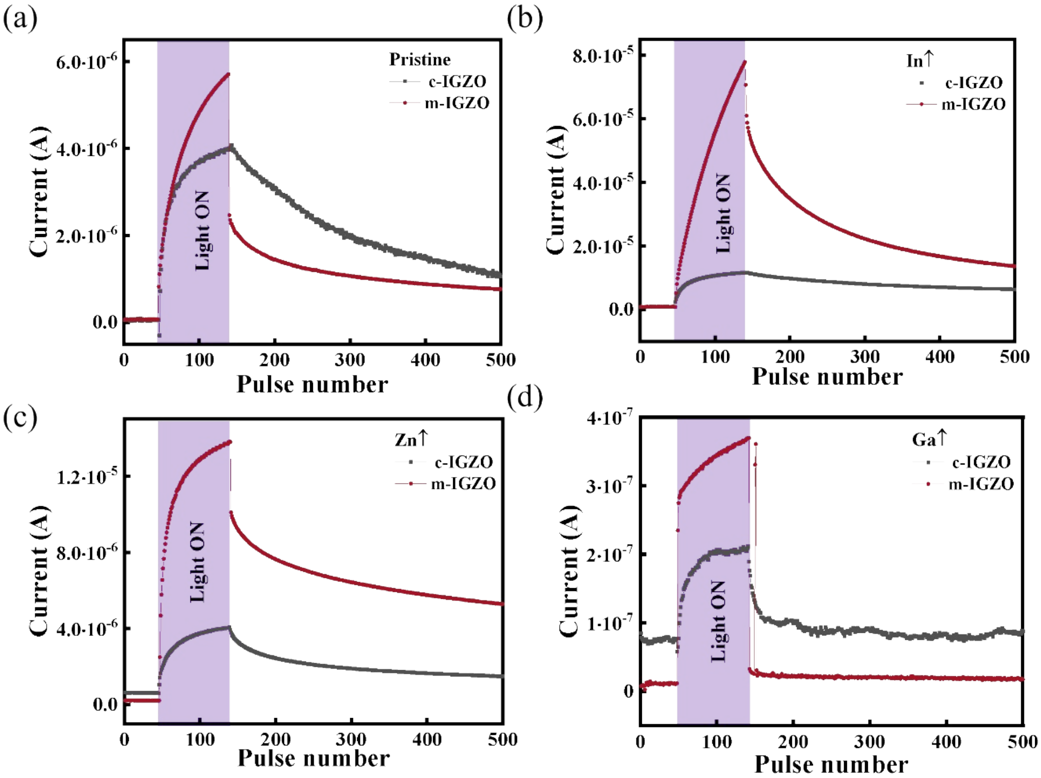

Figure S9. The comparison of current response under the light for 20 s of (a) pristine, (b) In↑, (c) Zn↑, and (d) Ga↑ c-IGZO and m-IGZO with the light intensities (1416 mW cm^{-2}), followed by current decay after light is off.

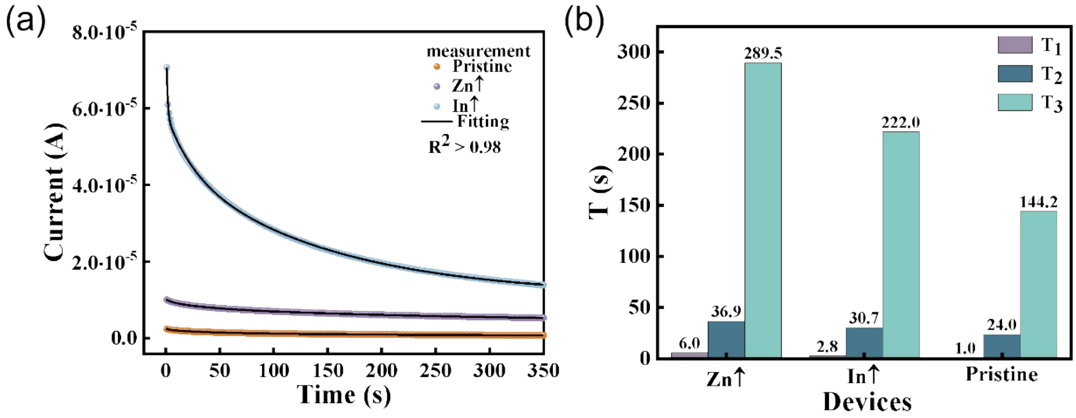

Figure S10. (a) Current decay curves and tri-exponential fitting for Zn↑, pristine, and In↑ devices. (b) Comparison of decay time constants for Zn↑, pristine, and In↑ devices.

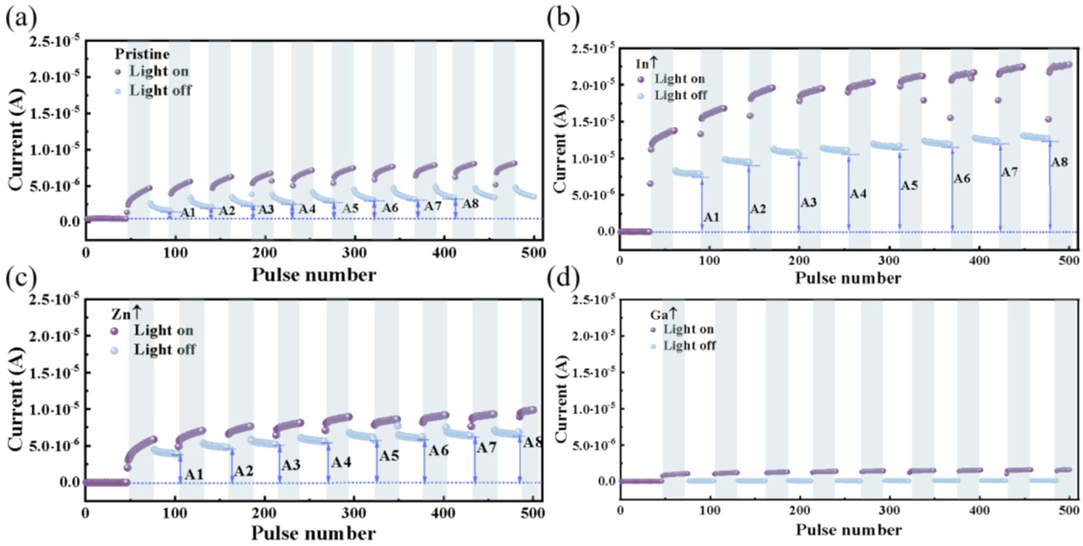

Figure S11. The current response of (a) pristine, (b) In↑, (c) Zn↑, (d) Ga↑ devices under consecutive light pulses.

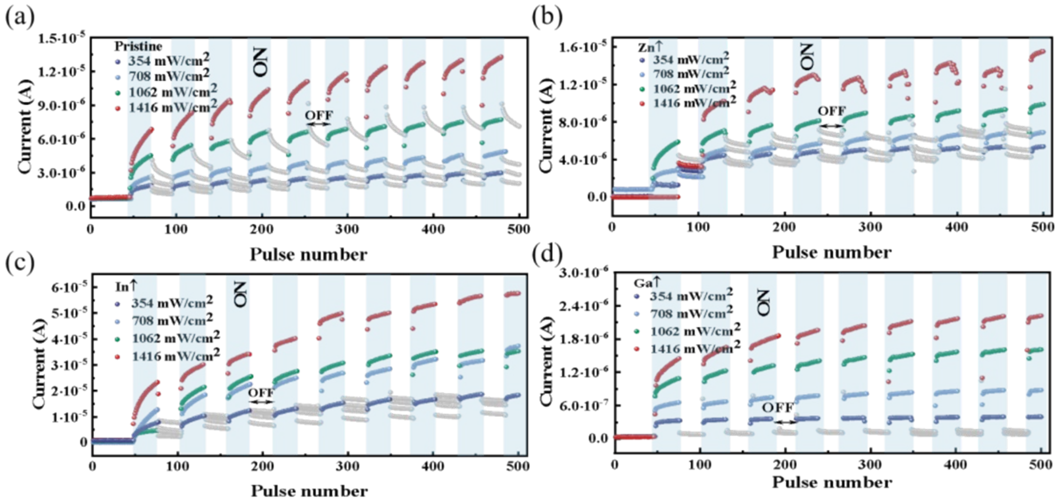

Figure S12. Current response of (a) pristine, (b) Zn↑, (c)In↑, (d) Ga↑ devices with various light intensities (354, 708, 1062, 1416 mW cm^{-2}) under consecutive light pulses.

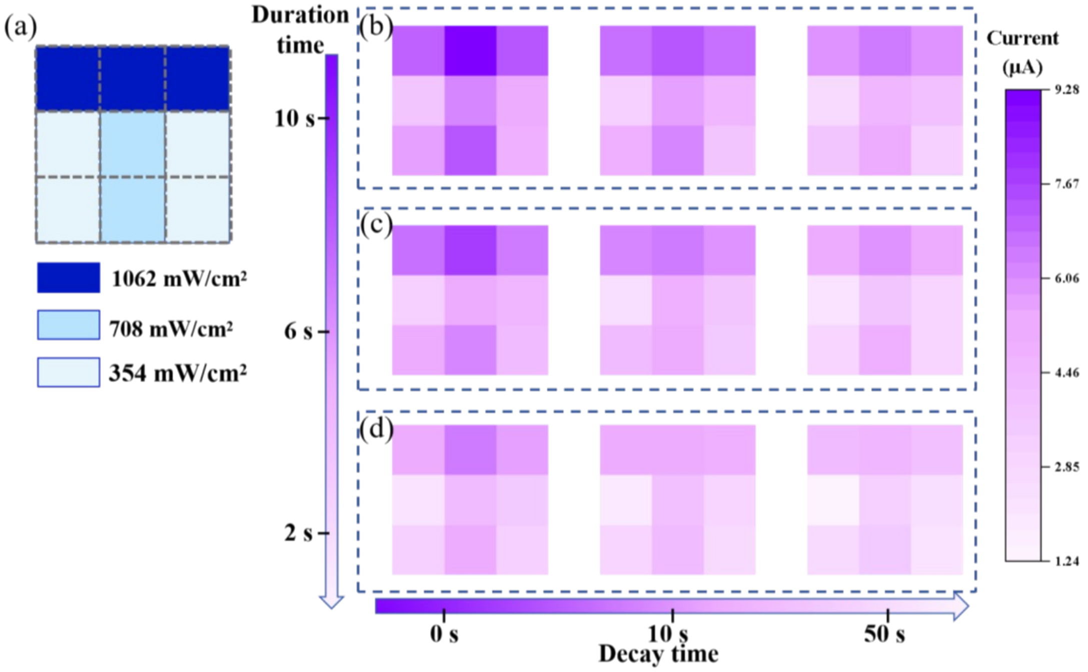

Figure S13. (a) Image mapping of the 3 × 3 array to various light intensities. The current response image mapping of the Zn↑ device with light duration times of (b) 10 s, (c) 6 s, and (d) 2 s.

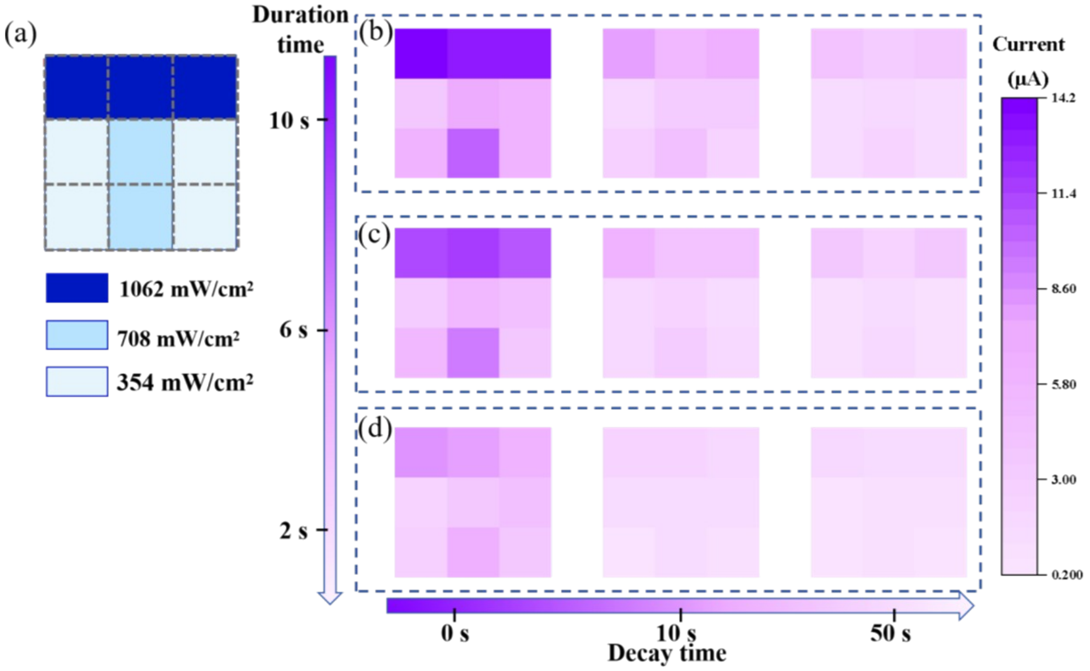

Figure S14. (a) Image mapping of the 3 × 3 array to various light intensities. The current response image mapping of the In↑ device with light duration times of (b) 10 s, (c) 6 s, and (d) 2 s.

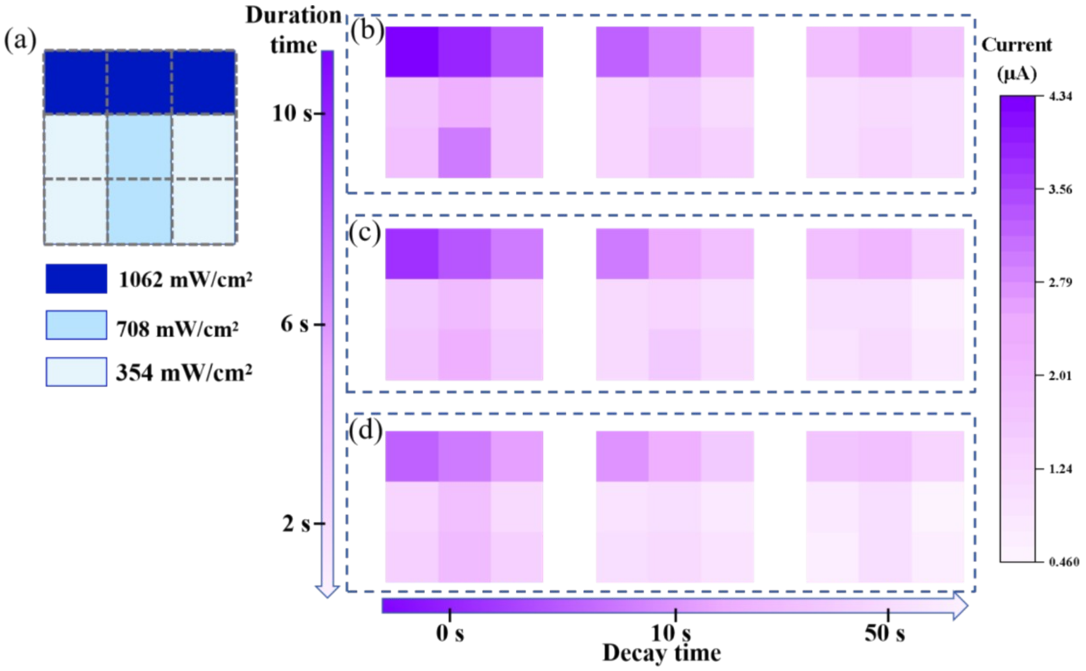

Figure S15. (a) Image mapping of the 3 × 3 array to various light intensities. The current response image mapping of the pristine device with light duration times of (b) 10 s, (c) 6 s, and (d) 2 s.

Figure S11-13(b), the current response of light irradiation with different intensities and the same duration of 10 s is different, and the predefined image “T” can be clearly seen by reading the current comparison. As the decay time increases, the current response gradually decreases to a low level that is not enough to recognize the image. Similar results can be obtained when the light pulse duration is 6 s and 2 s, as shown in Figure S11-13(c and b), respectively.

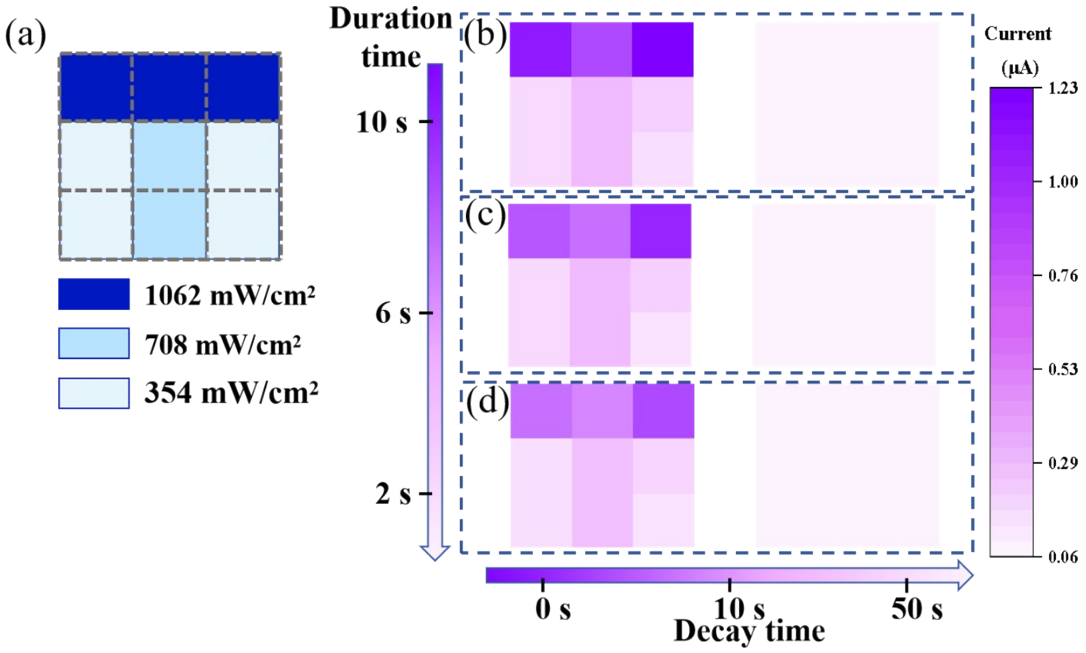

Figure S16. (a) Image mapping of the 3 × 3 array to various light intensities. The current response image mapping of the Ga↑ device with light duration times of (b) 10 s, (c) 6 s, and (d) 2 s.

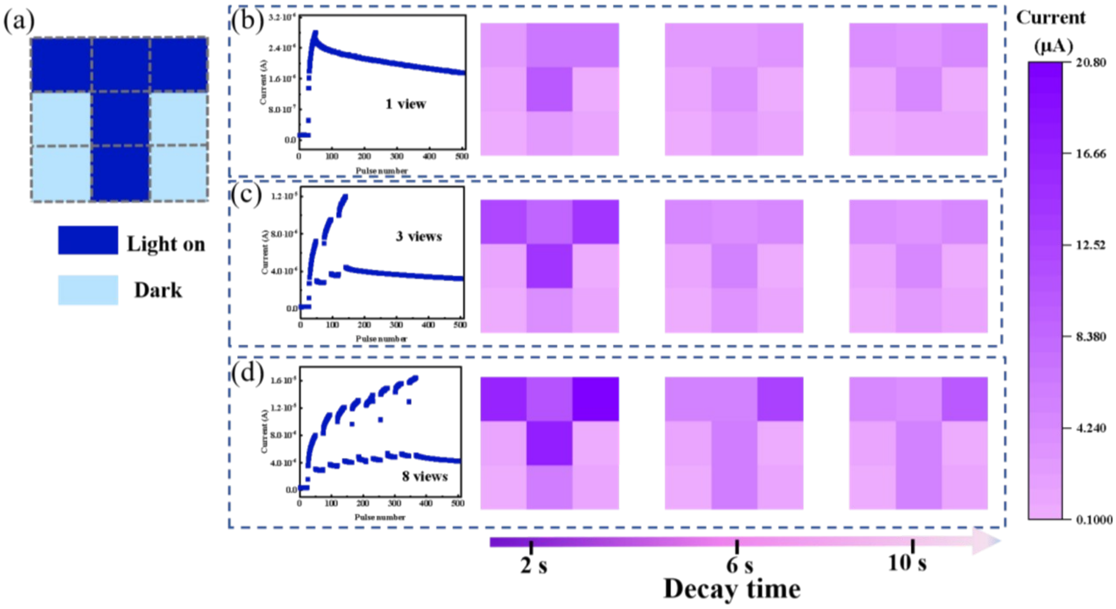

Figure S17. Emulation of visual memory function in a 3 × 3 array. (a) Image mapping of the 3 × 3 array to various views. The current response image mapping of the Zn↑ device after (b) 1 view, (c) 3 views, and (d) 8 views at 2 s, 6 s, and 10 s decay time.

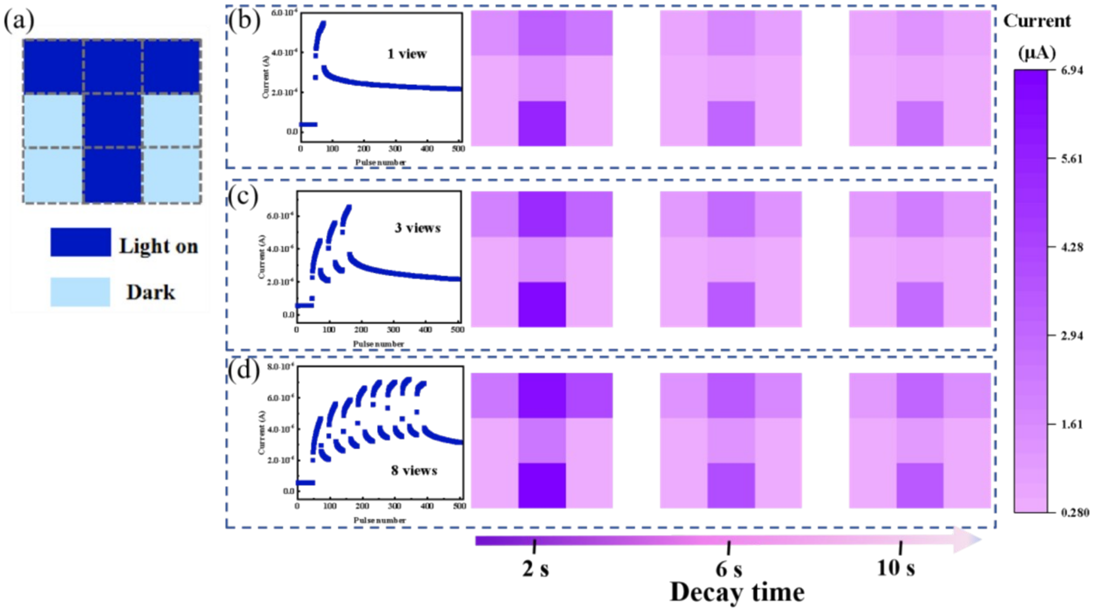

Figure S18. Emulation of visual memory function in a 3 × 3 array. (a) Image mapping of the 3 × 3 array to various views. The current response image mapping of the pristine device after (b) 1 view, (c) 3 views, and (d) 8 views at 2 s, 6 s, and 10 s decay time.

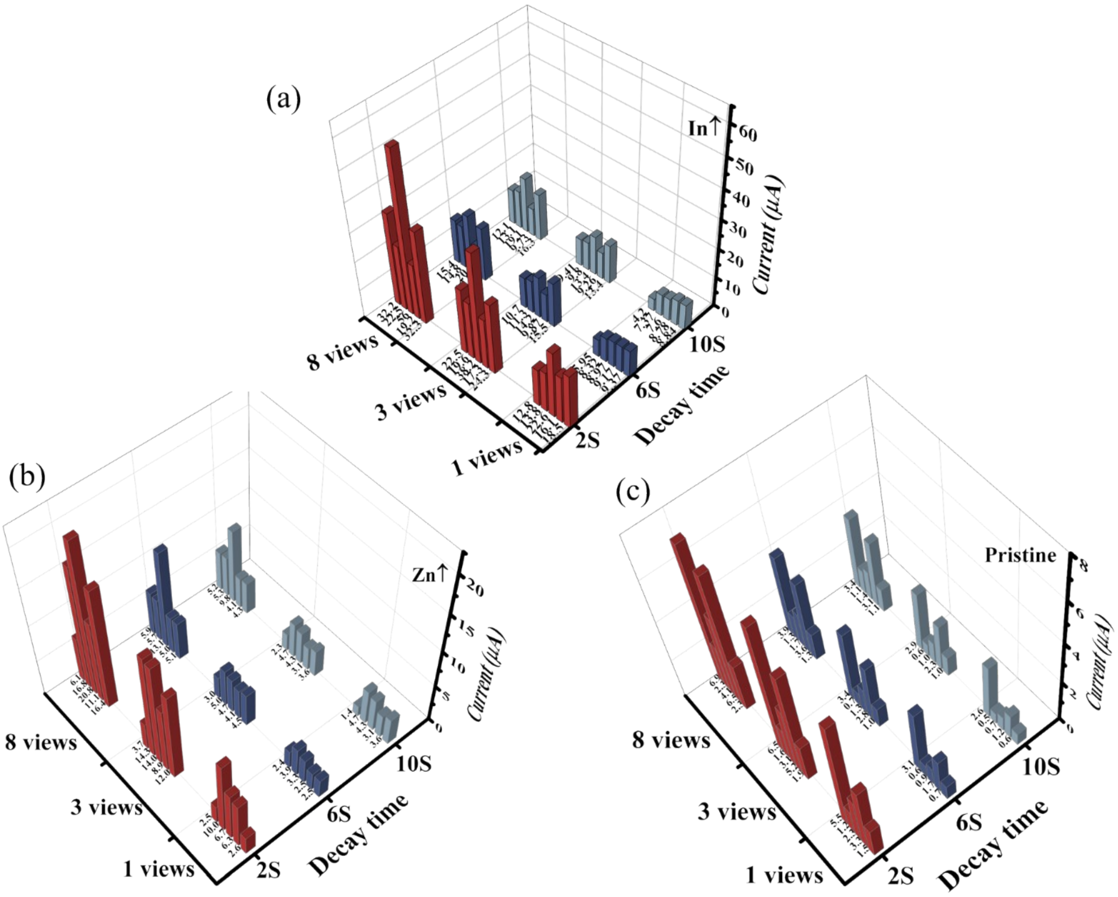

Figure S19. The quantitative data of the visual memory effect (a) In↑, (b) Zn↑ and (c) pristine devices at decay times of 2 s, 6 s, and 10 s after 1, 3, and 8 viewing cycles.

Table S2. Comparison of the Photoresponse Parameters of the Ga↑ device from this work and other previously reported photodetectors.

photodetector	Wavelength (nm)	I_{photo}/I_{dark} ratio	rise time/decay time	Responsivity (mA/W)	ref
Ga_2O_3/NSTO	254	20	0.21 s/0.07 s	2.6	[1]
ZnO/Ga_2O_3	251		100 μs/900 μs	9.7	[2]
GaN/Ga_2O_3	254	80	0.14 s/0.07 s	28.44	[3]
AZNF	365	100	37 ms/330ms	0.039	[4]
β-Ga_2O_3/NiO	284		0.49 s/0.14 s	10	[5]
α-Ga_2O_3/Ti	254		0.104 s/0.077 s	15.3	[6]
CeO_2	356	15.2	183 ms/3 ms	227.7	[7]
β-Ga_2O_3/Pt	265		1.78 s/2.09 s	0.0116	[8]
Ga↑	356	26	0.39 s/0.12 s	3.63	this work

Although the Ga↑ device in this work shows similar performance compared to the recent works, it shows potential as a better future UV photodetector with systematic optimization. Herein, we decrease the thickness of the film to 130 nm and increase the optical response of the device to 1×10^{-6} A, as shown in Figure S22. This result also sheds some light on the optimization of the fabrication of IGZO-based UV photodetectors. Especially in terms of optimizing the thickness of the film.

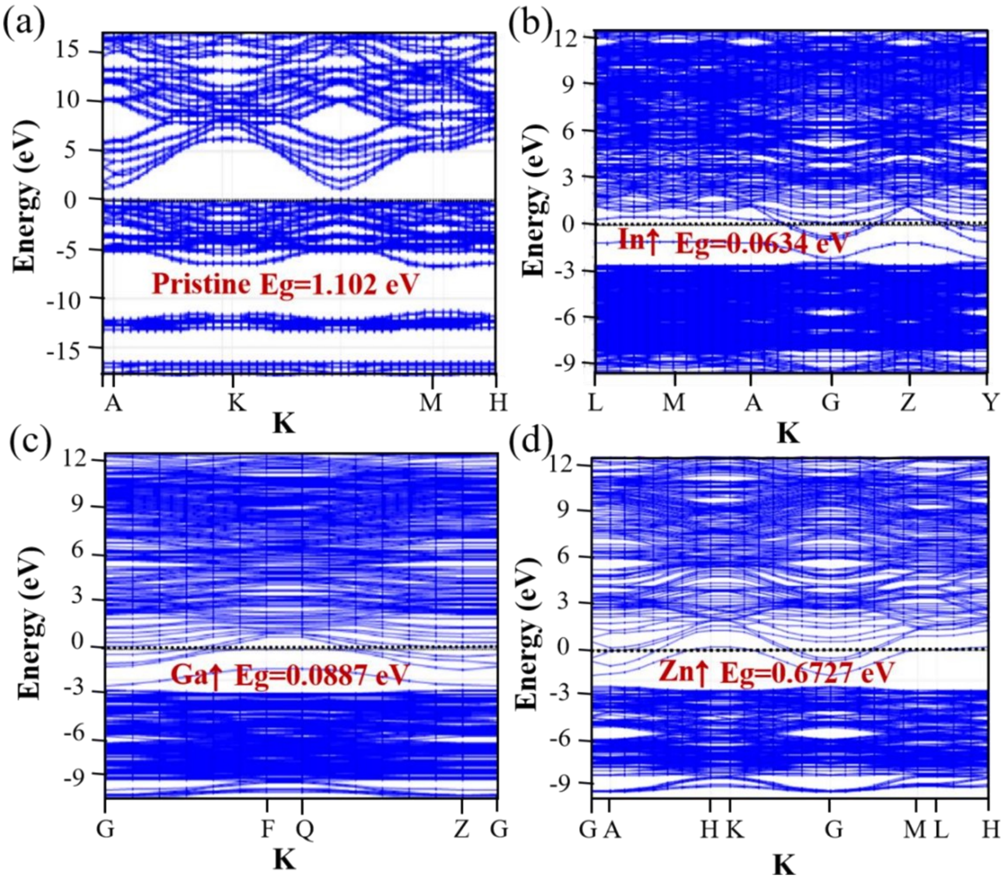

Figure S20. The computational band structures of (a) pristine, (b) In↑, (c) Ga↑, and (d) Zn↑ devices.

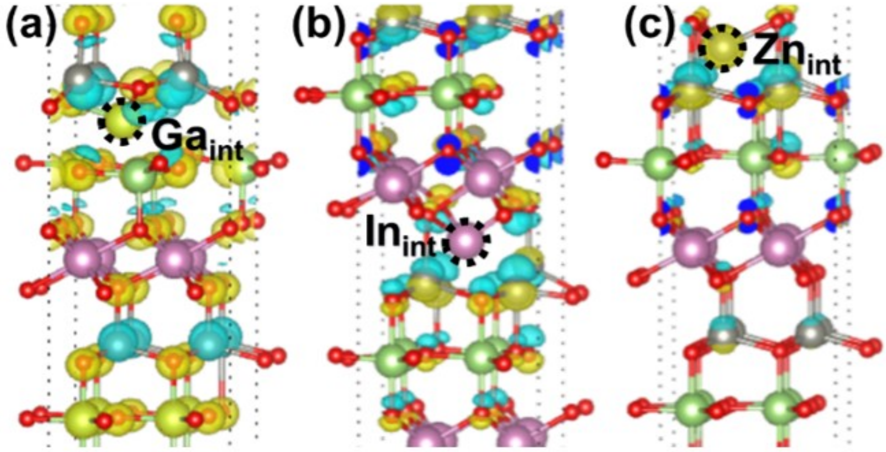

Figure S21. Electron density difference diagrams of IGZO with (a) interstitial gallium, (b) interstitial indium, and (c) interstitial zinc.

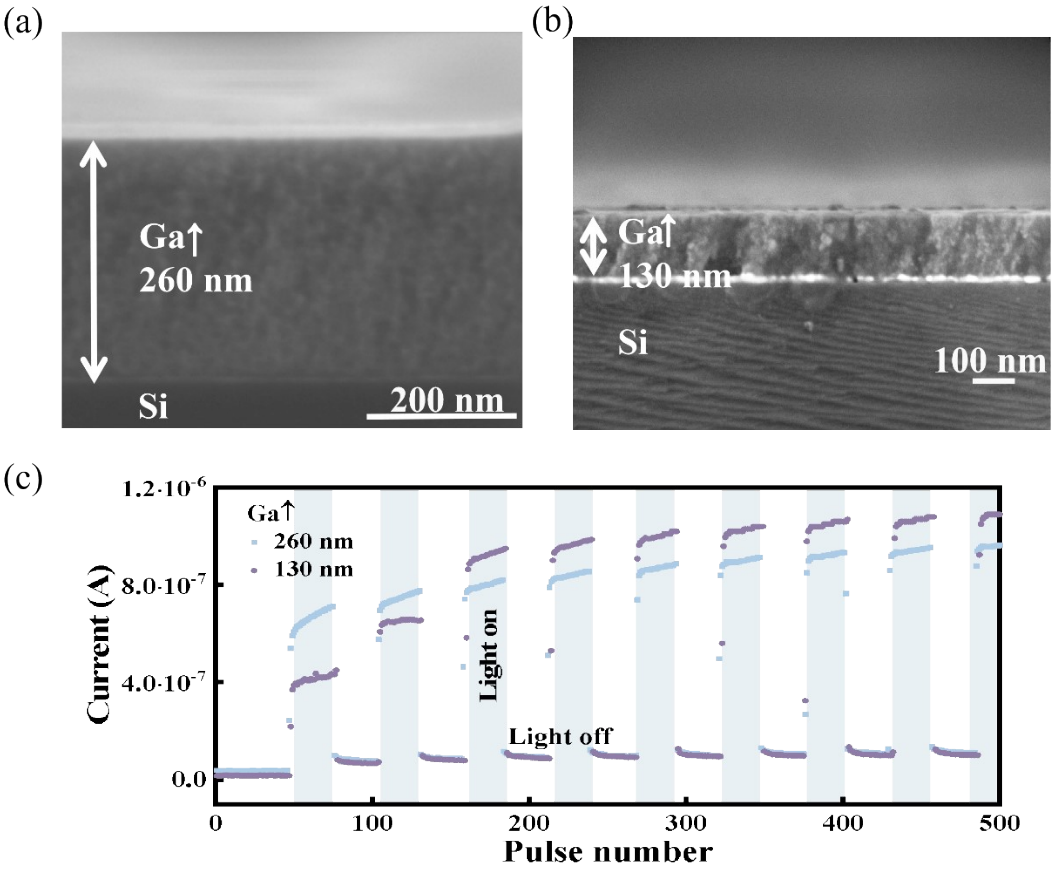

Figure S22. Cross-sectional SEM image of the film thicknesses of Ga↑ devices with film thicknesses of 260 nm (a) and 130 nm (b); (c) The comparison of photocurrent responses of Ga↑ devices with film thicknesses of 130 nm and 260 nm under continuous light pulses.

As shown in Figure S22(c), it can be seen that although the device with a 260nm film thickness has a slightly lower light response compared to the 130nm one, its volatility remains. Herein, we increased the optical response of the device to 1×10^{-6} A. This result also sheds some light on the optimization of the fabrication of IGZO-based UV photodetectors. Especially in terms of optimizing the thickness of the film.

References

1. Chen X, Xu Y, Zhou D, et al. Solar-Blind Photodetector with High Avalanche Gains and Bias-Tunable Detecting Functionality Based on Metastable Phase α-Ga_2O_3/ZnO Isotype Heterostructures. ACS Applied Materials & Interfaces. 2017;9: 36997-37005.
2. Liu Y, Jia R, Wang Y, et al. Inhibition of Zero Drift in Perovskite-Based Photodetector Devices via 6,6 -Phenyl-C61-butyric Acid Methyl Ester Doping. ACS Applied Materials & Interfaces. 2017;9: 15638-15643.
3. Chen X, Liu K, Zhang Z, et al. Self-Powered Solar-Blind Photodetector with Fast Response Based on Au/β-Ga_2O_3 Nanowires Array Film Schottky Junction. ACS Applied Materials & Interfaces. 2016;8: 4185-4191.
4. Duan L, He F, Tian Y, et al. Fabrication of Self-Powered Fast-Response Ultraviolet Photodetectors Based on Graphene/ZnO:Al Nanorod-Array-Film Structure with Stable Schottky Barrier. ACS Applied Materials & Interfaces. 2017;9: 8161-8168.
5. Tang X, Lu Y, Lin R, et al. Flexible self-powered DUV photodetectors with high responsivity utilizing Ga_2O_3/NiO heterostructure on buffered Hastelloy substrates. Applied Physics Letters. 2023;122: 121101.
6. Chen Z, Han P, Chen W, et al. Flexible and Self-Powered Solar-Blind UV Photodetector Based on the Ti/α-Ga_2O_3/Electrolyte Heterojunction with High Stability. ACS Applied Electronic Materials. 2023;6: 496-504.
7. Zhang J, Wang Y, Guan P, et al. The overlooked cation interstitials in optimizing UV photodetectors: A case study in CeO_2-based. Journal of Alloys and Compounds. 2025;1040.
8. Tak BR, Yang M-M, Lai Y-H, Chu Y-H, Alexe M, Singh R. Photovoltaic and flexible deep ultraviolet wavelength detector based on novel β-Ga_2O_3/muscovite heteroepitaxy. Scientific Reports. 2020;10.